

## Characterisation of SuperNEMO demonstrator calorimeter timing performance Study of $^{208}\text{TI}$ background rejection influence on the $0\nu\beta\beta$ decay sensitivity

Thèse de doctorat de l'Université Paris-Saclay  
préparée à l'Université Paris Saclay au sein du Laboratoire Irène-Joliot Curie  
(anciennement Laboratoire de l'Accélérateur Linéaire)

École doctorale n°576 Particles, Hadrons, Energy, Nuclei,  
Instrumentation, Imaging, Cosmos et Simulation (PHENIICS)  
Spécialité de doctorat : Physique des particules

Thèse présentée et soutenue à Orsay, le 11 décembre 2020, par

**CLOÉ GIRARD-CARILLO**

### Composition du Jury :

Alessandra Tonazzo APC - Paris	Rapporteure
Mark C. Chen Queen's University	Rapporteur
Christine Marquet CENBG - Bordeaux-Gradignan	Examinatrice
Achille Stocchi LAL - Orsay	Examineur
Laurent Simard LAL - Orsay	Directeur de thèse
Mathieu Bongrand LAL - Orsay	Co-directeur de thèse





---

# Contents

Acknowledgement	3
Contents	5
Introduction	9
<b>1 Phenomenology of particle physics</b>	<b>11</b>
1.1 The Standard Model of particle physics . . . . .	11
1.1.1 Bosons . . . . .	11
1.1.2 Fermions . . . . .	11
1.1.3 $2\nu\beta\beta$ decay . . . . .	11
1.1.4 Where the Standard Model ends . . . . .	11
1.2 Going beyond the Standard Model with neutrinos . . . . .	11
1.2.1 Neutrino flavors and oscillations . . . . .	11
1.2.2 Neutrino masses and nature . . . . .	11
1.2.3 Neutrinoless double beta decay . . . . .	11
1.2.4 Other searches beyond the Standard Model with neutrinos .	11
1.3 $0\nu\beta\beta$ experiment status . . . . .	11
1.3.1 Experimental design criteria . . . . .	11
1.3.2 $0\nu\beta\beta$ direct search experiments . . . . .	13
1.3.3 Bolometers . . . . .	14
1.3.4 Time projection chambers . . . . .	14
1.3.5 Scintillators . . . . .	15
1.3.6 Tracking calorimeters . . . . .	17
<b>2 The SuperNEMO demonstrator</b>	<b>19</b>
2.1 The SuperNEMO technology . . . . .	20
2.1.1 Detection principle . . . . .	20
2.1.2 The source foils . . . . .	22
2.1.3 The tracker . . . . .	25
2.1.4 The calorimeter . . . . .	29
2.1.5 The magnetic coil and the shieldings . . . . .	34
2.1.6 Calibration strategy . . . . .	35

2.1.7	Detector cabling . . . . .	37
2.1.8	Electronics . . . . .	39
2.1.9	Detector gas tightness . . . . .	42
2.2	Backgrounds . . . . .	43
2.2.1	Internal background . . . . .	44
2.2.2	External background . . . . .	46
2.2.3	Radon background . . . . .	47
2.2.4	Background reduction . . . . .	48
2.3	The SuperNEMO software . . . . .	48
2.3.1	Simulation . . . . .	49
2.3.2	Reconstruction pipeline . . . . .	49
2.3.3	Analysis tools . . . . .	50
2.4	Conclusion . . . . .	53
<b>3</b>	<b>Sensitivity of the SuperNEMO demonstrator to the <math>0\nu\beta\beta</math></b>	<b>55</b>
3.1	The $0\nu\beta\beta$ signal and background model . . . . .	55
3.1.1	The $0\nu\beta\beta$ signal . . . . .	56
3.1.2	Inside detector backgrounds . . . . .	56
3.1.3	External backgrounds . . . . .	57
3.1.4	Expected number of decays . . . . .	58
3.2	Event selection . . . . .	59
3.2.1	Electron definition . . . . .	59
3.2.2	Total energy spectrum . . . . .	59
3.3	Demonstrator sensitivity to the $0\nu\beta\beta$ decay of $^{82}\text{Se}$ . . . . .	61
3.3.1	Sensitivity to the $0\nu\beta\beta$ half-life . . . . .	61
3.3.2	Limit on the effective neutrino mass . . . . .	63
3.4	Impact of sources contamination levels on the sensitivity . . . . .	65
3.4.1	Contamination levels . . . . .	65
3.4.2	Optimisation of event selection . . . . .	68
3.5	Impact of the magnetic field on the sensitivity . . . . .	74
3.5.1	Simulations of the magnetic field inside the demonstrator and reconstructed track fit . . . . .	74
3.5.2	Impact of the magnetic field on signal and background selections . . . . .	75
3.5.3	Influence of the magnetic field on optical modules and reconstruction efficiency . . . . .	77
3.5.4	Simulations with a non-uniform magnetic field . . . . .	78
3.6	Searching for the Neodymium-150 $0\nu\beta\beta$ decay . . . . .	80
3.6.1	Searching for the $0\nu\beta\beta$ of other isotopes . . . . .	80
3.6.2	Sensitivity to the $0\nu\beta\beta$ of $^{150}\text{Nd}$ . . . . .	80
3.7	The final detector sensitivity . . . . .	82
3.8	Conclusion . . . . .	83
<b>4</b>	<b>Improvement of the internal Thallium-208 background rejection</b>	<b>87</b>
4.1	Motivations . . . . .	87
4.2	The internal $^{208}\text{Tl}$ background . . . . .	88
4.2.1	The internal conversion process . . . . .	89

4.2.2	$^{208}\text{Tl}$ disintegrations in the 2e channel . . . . .	90
4.3	Simulated demonstrator performances . . . . .	91
4.4	Rejection of $^{208}\text{Tl}$ with a time-of-flight criterion . . . . .	92
4.4.1	The internal probability . . . . .	92
4.4.2	The exponential probability for $^{208}\text{Tl}$ events . . . . .	94
4.5	Event selection . . . . .	96
4.5.1	Energy selection . . . . .	97
4.5.2	Time-of-flight cut-off . . . . .	97
4.5.3	Probability cut-off . . . . .	99
4.5.4	Influence of the calorimeter time resolution . . . . .	102
4.6	Impact of $^{208}\text{Tl}$ rejection on the experiment's sensitivity . . . . .	105
4.7	Conclusion . . . . .	106
<b>5</b>	<b>Characterisation of the calorimeter time resolution</b>	<b>107</b>
5.1	Interaction of particles in the SuperNEMO scintillators . . . . .	108
5.1.1	Interaction of electrons . . . . .	108
5.1.2	Interaction of photons . . . . .	108
5.2	Measurement of the time resolution with a $^{60}\text{Co}$ source . . . . .	109
5.2.1	Description of Cobalt 60 nucleus . . . . .	110
5.2.2	Time response of optical modules . . . . .	110
5.2.3	Final experimental design . . . . .	113
5.2.4	Signal events selection . . . . .	115
5.2.5	Background estimation . . . . .	117
5.2.6	Detector efficiency . . . . .	121
5.2.7	Determination of the individual timing resolution of each optical module . . . . .	121
5.2.8	Conclusion . . . . .	126
5.3	The Light Injection System . . . . .	126
5.3.1	Light injection system commissioning . . . . .	126
5.3.2	Time resolution of optical modules . . . . .	126
<b>6</b>	<b>Detector commissioning</b>	<b>129</b>
6.1	Reflectometry analysis . . . . .	129
6.1.1	Goal of the reflectometry analysis . . . . .	129
6.1.2	Pulse timing: controlling cable lengths . . . . .	130
6.1.3	Signal attenuation . . . . .	134
6.1.4	Pulse shape analysis . . . . .	136
6.1.5	Comparison with $^{60}\text{Co}$ . . . . .	137
6.1.6	Conclusion . . . . .	137
6.2	Calibrating the electronic boards . . . . .	137
6.2.1	Principle . . . . .	137
6.2.2	Measuring the time offset of front end boards . . . . .	137
6.2.3	Results . . . . .	137
6.3	Energy calibration of optical modules . . . . .	137
6.4	Baseline studies . . . . .	137
6.5	Light Injection System . . . . .	137

## CONTENTS

---

<b>Conclusion</b>	<b>139</b>
<b>Résumé</b>	<b>141</b>
<b>Bibliography</b>	<b>143</b>





## Improvement of the internal Thallium-208 background rejection

At the end of September 2018, the 34 enriched-Selenium source foils were installed on the demonstrator. At this time, the internal  $^{208}\text{Tl}$  and  $^{214}\text{Bi}$  activities of these sources had already been measured by the BiPo detector. Also, the Radon concentration in the chamber was extrapolated from Radon emission measurements of the tracker components with a concentration line for an incoming gas flow of  $2 \text{ m}^3/\text{h}$ . We described in the previous chapter the impact of these activities on the final detector sensitivity to the  $0\nu\beta\beta$  decay, and set up optimised topological selections adjusted to reject the Radon background.

However,  $^{208}\text{Tl}$  disintegrations in the sources also remains a troublesome background, even for  $\beta\beta$  emitters with a high  $Q_{\beta\beta}$ . Indeed, it contributes at high energies (up to 4 MeV on the two electrons energy sum spectrum), because of the internal conversion of the 2.615 MeV  $\gamma$ -ray. In a context where the  $^{208}\text{Tl}$  contamination is higher than expected inside the sources, we focus in the current chapter on rejection techniques peculiarly adapted to reject internal  $^{208}\text{Tl}$  events. We study the influence of these additional techniques on  $0\nu\beta\beta$  events selection, and evaluate the impact on final detector sensitivity. Impact of the calorimeter timing performances on these techniques are also addressed in this chapter.

### 4.1 Motivations

In Chapters 2 and 3, we presented the specifications set on the background activities, in order to reach the target limit on the  $0\nu\beta\beta$  process half-life of the  $^{82}\text{Se}$  in 5 years, with 100 kg of isotope. The Tab. 2.3 given in Chapter 2 summarises the target  $^{208}\text{Tl}$ ,  $^{214}\text{Bi}$  and  $^{222}\text{Rn}$  activities, and provides a comparison with those measured by the collaboration. The BiPo detector was capable of giving an upper limit on the  $^{214}\text{Bi}$  level of  $\mathcal{A}^{\text{Bi}} < 290 \text{ } \mu\text{Bq/kg}$  at 90% CL, and future more precise measurements with SuperNEMO demonstrator will constraint this value. The BiPo measurements also showed that the  $^{208}\text{Tl}$  contamination is about 30 times greater than expected on average. We give in Tab. 4.1 the number of expected background events for the measured activities (taking the upper limit for  $^{214}\text{Bi}$

#### 4. IMPROVEMENT OF THE INTERNAL THALLIUM-208 BACKGROUND REJECTION

contamination), for the demonstrator and final detector. The  $^{208}\text{Tl}$  level of activity

Exposure ROI (MeV)	Demonstrator 17.5 kg.y [2.7;3.3]	Detector 500 kg.y [2.6;2.95]
$2\nu\beta\beta$	0.383	104
$^{208}\text{Tl}$	1.09	21.2
$^{214}\text{Bi}$	1.42	110
$^{222}\text{Rn}$	0.0782	6.11

Table 4.1: Expected number of background events in the  $2e$  topology, in optimised energy ranges for the SuperNEMO demonstrator (17.5 kg.y) and the final detector (500 kg.y exposure). The  $2\nu\beta\beta$  half-life is taken as  $T_{1/2}^{2\nu} = 9.39 \times 10^{19}$  y, and the measured background activities are considered (with the upper limit for  $^{214}\text{Bi}$  contamination). The topological selections have been optimised:  $P_{int} > 4\%$  and  $|\Delta Z| < 80$  mm.

has no implication for the demonstrator (17.5 kg.y exposure), as only one event is expected in the optimised [2.7;3.3] MeV energy region, after first-order and topological cut-offs were applied. On the other hand, this background could be harmful for the final detector (500 kg.y exposure), with 21 events expected in the region of interest [2.6,2.95] MeV. To overcome this effect, it is interesting to set a specific method designed to reject  $^{208}\text{Tl}$  events.

In the next section, we describe the specific features of the Thallium internal background. We develop a new technique of rejection, especially designed to identify internal  $^{208}\text{Tl}$  events, based on several Time-Of-Flight computations.

## 4.2 The internal $^{208}\text{Tl}$ background

As described in Chapter 2, radioactive isotope disintegrations inside the source foils can occasionally produce two-electron events, and thus can mimic  $\beta\beta$ -decay events. The  $^{208}\text{Tl}$ , a progeny of  $^{232}\text{Th}$ , is one of the largest contribution to the internal background. Two electrons can be produced via a  $\beta$ -decay followed by a Møller scattering,  $\beta$ -decay to an excited state with the subsequent internal conversion, or due to Compton scattering of the de-excitation photon.

The disintegration scheme of  $^{208}\text{Tl}$  isotope is presented in Fig. 4.1. This shows that  $^{208}\text{Tl}$  always  $\beta$ -decays to an excited state of the  $^{208}\text{Pb}$  daughter nuclei. In more than 99 % of the decays, at least 2  $\gamma$ 's are expected after the  $\beta$  emission. For  $0\nu\beta\beta$  detection of isotopes with high  $Q_{\beta\beta}$ , the most dangerous mode of  $\beta\beta$ -like events production comes from the internal conversion of the 2.615 MeV- $\gamma$ , resulting in one electron with an energy of 2.5 MeV approximately and a beta-electron with a continuous spectrum between 0 and  $\sim 1.5$  MeV. Thus  $^{208}\text{Tl}$  events with a total energy greater than 2.7 MeV can populate the region of interest.

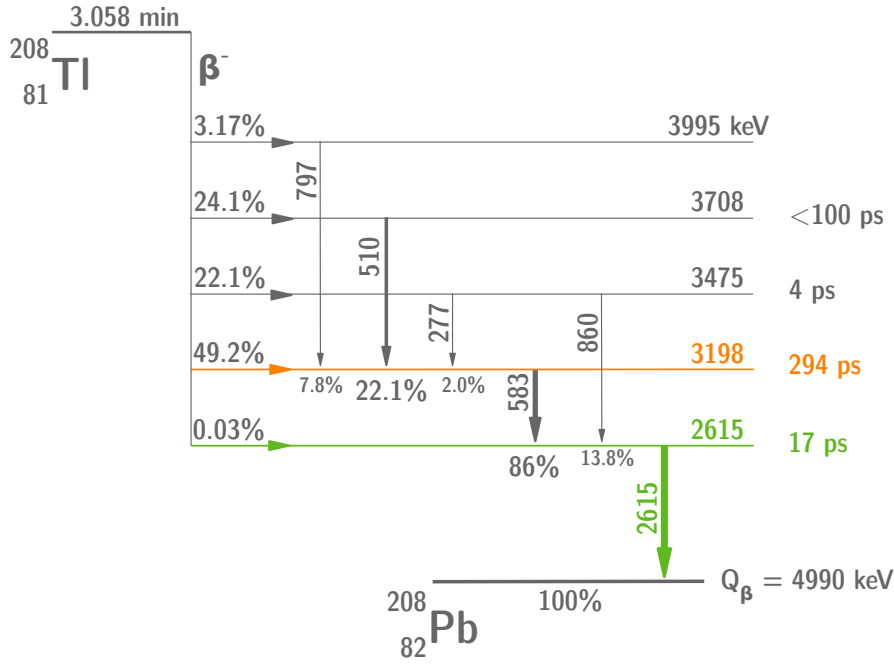


Figure 4.1: A simplified disintegration scheme for the  $^{208}\text{Tl}$  isotope. 81 % of the disintegration pass through the 294 ps metastable energy level (orange). All disintegration go through the 2.615 MeV energy level (green), where an orbital electron is ejected in 0.246 % of the cases through the internal conversion process.

#### 4.2.1 The internal conversion process

An excited nucleus will practically constantly achieve a transition to a lower state by one of two processes: the emission of a  $\gamma$ -ray, or the ejection of one of the orbital electrons. The latter, called *internal conversion* (frequently abbreviated IC), is a second-order process, where one electron couples to one of the proton inside the excited nucleus. Thus, in such a radioactive decay, the de-excitation energy of the nucleus is transferred *directly* to a  $j$ -shell electron ( $j = K, L, M \dots$ ). A high-energy electron is therefore emitted from the atom, and carry off the energy

$$E_{IC} = E_\gamma - E_j \quad (j = K, L, M \dots), \quad (4.1)$$

where  $E_j$  is the binding energy of the electron in the  $j$ -shell, and  $E_\gamma$  is the energy of the  $\gamma$ -ray.

This mechanism is possible because there is a non-zero probability of finding the electron within the nucleus, that is to say, the wave-function of the electron can penetrate the volume of the nucleus. Consequently, due to their high nuclear penetration, electrons coming from the  $1s$  state are more likely to be ejected (this transition is called  $K$  internal conversion). Although electrons coming from  $2s$ ,  $3s$  and  $4s$  states ( $L$ ,  $M$  or  $N$  internal conversions) have also a non-zero probability to undergo this process. After the electron ejection, the hole in the corresponding shell is filled by an electron from a higher energy level, emitting characteristic X-rays, Auger electrons, or both.

For a given transition, the internal conversion coefficient of the electron in the  $j$ -shell, is defined by

$$\alpha_j = \frac{P_{IC,j}}{P_\gamma}, \quad (4.2)$$

where  $P_{IC,j}$  is the  $j$  conversion electron emission probability, and  $P_\gamma$  is the  $\gamma$ -ray emission probability. The total coefficient is

$$\alpha_T = \sum_{j=K,L,M\cdots} \alpha_j. \quad (4.3)$$

These coefficients are given in Tab. 4.2 for the 2.615 MeV energy level of  $^{208}\text{Tl}$  isotope. Therefore, in 0.246 % of the cases, the  $^{208}\text{Pb}$  excited nucleus will

$j$ -shell	$K$	$L$	$M$	Total
IC coefficients (%)	0.1708	0.0292	0.00685	0.246

Table 4.2: Internal conversion coefficients for the 2.615 MeV  $\gamma$ -ray of the  $^{208}\text{Tl}$  decay scheme.

undergone an internal conversion corresponding to the 2.615 MeV energy level.

#### 4.2.2 $^{208}\text{Tl}$ disintegrations in the 2e channel

Finally, a  $^{208}\text{Tl}$  decay can present a two-electrons topology when, after the  $\beta$  emission, an electron is ejected from the atom through internal conversion. Especially, when this energy transfer corresponds to the 2.615 MeV  $\gamma$ -ray, the ejected electron carry off a significant energy, depending on its initial binding energy with the nucleus. For instance an orbital electron from the  $K$ -shell is ejected with an energy  $E_{IC,K} = 2.526$  MeV ( $\alpha_K = 0.17\%$ ). This decay is therefore likely to contribute in the region of interest for the  $0\nu\beta\beta$  search of  $^{82}\text{Se}$ , or even  $^{150}\text{Nd}$ .

In the 2e channel, optimised topological cut-offs, based on time-of-flight computation and the distance between vertices, were presented in the previous chapter. They are mostly efficient in rejecting the non-internal  $^{222}\text{Rn}$  events. After a brief presentation of the simulations carried out as part of this analysis, we remind and precise the internal probability computation, and present a new selection, also based on the time-of-flight computation, to reject the  $^{208}\text{Tl}$  background.

- donner la proportion d'ev retardés avec la bank SD (simus en train de tourner)
- relire et compléter cette sous-section
- Avant d'entrer dans le détail préciser le principe de la réjection par temps de vol. L'électron de plus haute énergie est en retard, avec un retard en moyenne de 294 ps pour la plupart des niveaux (discuter un peu le schéma de désintégration, dans quel cas il sera en retard). Ensuite dire que tu as quantifié le pourcentage d'électrons de haute énergie en retard

avec une simulation "parfaite" i.e. avec une résolution en temps nulle. A comparer avec le chiffre donné précédemment (issu d'une étude du schéma de désintégration.)

### 4.3 Simulated demonstrator performances

The background model used in the framework of this study has already been described in detail in the previous chapter. Nevertheless, calorimeter performances implemented in the Falaise software have been modified in this study. Indeed, one of the main goal is to evaluate the influence of the calorimeter timing performances on the  $^{208}\text{Tl}$  background rejection. This study was led before the commissioning phase of the calorimeter when timing performances were characterised only for few optical modules, and before their installation at Modane [15]. An encouraging value for the uncertainty on the calorimeter time measurement of 251.1 ps for incoming electrons and 393.2 ps for photons were provided for the best optical module tested (Fig. 4.2). In this context, before the full calorimeter calibration

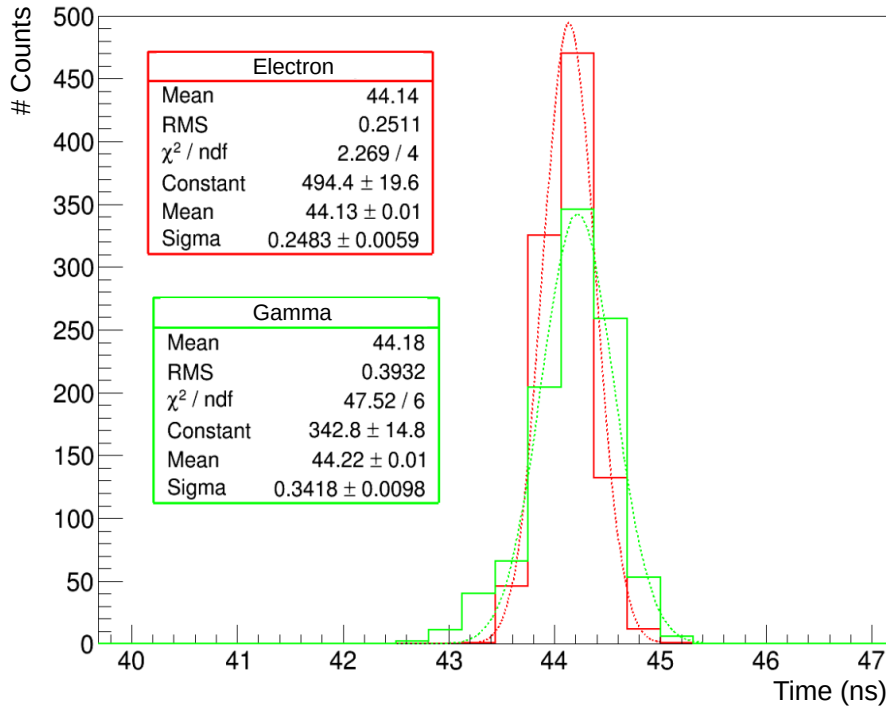


Figure 4.2: Time distribution of the trigger time of an optical module in the case of electrons (red) and gamma radiation (green) depositing an energy of 1 MeV in the scintillator. The trigger threshold is set at 45 mV and corresponds to an energy of 0.150 MeV. Adapted from [15].

in Modane, we would give an overview of the influence of these performances on the  $^{208}\text{Tl}$  background rejection. To do so, signal and background simulations were performed supposing the optical modules measure perfectly the particle time-of-flights, by setting to zero the time uncertainty at the level of the calibration module

in the Falaise pipeline. I wrote a Root code allowing to degrade the precision on time measurements for it to be set by the user to the desired accuracy.

All of the simulations produced for this analysis were generated using the official Falaise pipeline, and are made available to the collaboration in the common SuperNEMO repository at CC Lyon. The same code described in the previous chapter has been used for this study, including the Particle Identification module, the module I wrote and the Root code pipeline. An additional set of codes have been developped in order to degrade the simulated calorimeter resolution as well as to compute the analysis tools decribed in the following.

In the first instance we set the reasonable value of 200 ps for the measurement uncertainty. In Sec. 4.5.4 the influence of this parameter on the  $^{208}\text{Tl}$  rejection is provided, and we give final sensitivity results according to it in Sec. 4.6.

## 4.4 Rejection of $^{208}\text{Tl}$ with a time-of-flight criterion

The internal probability, based on time-of-flight computation, quantifies the likelihood that two particles were amitted inside the source foils, from the same vertex. Unless it is a useful tool, we would implement a new one, also based on time-of-flights, taking into account the possible delay between the two incomming electrons due to the  $^{208}\text{Tl}$  metastable state.

### 4.4.1 The internal probability

As part of the analysis pipeline, this tool is widely employed in NEMO-3 and SuperNEMO, for background rejection purposes. We present it in detail in Chapter 2 and examine an example of its usefulness in Chapter 3. Nevertheless, in the framework of this analysis we need to perform our own calculation of internal probability, after the reconstruction pipeline, because the simulations are performed for an ideal value of the optical module performances. That is an opportunity to come back to this tool and to clarify certain points.

The calculation of the internal  $\chi^2$  is reminded in Eq. (4.4), for two detected electrons, as a function of the expected time-of-flights,  $t^{\text{exp}}$ , the experimentally measured time-of-flights,  $t^{\text{meas}}$ , as well as the total uncertainty on the time-of-flight measurement:

$$\chi_{int}^2 = \frac{((t_1^{\text{meas}} - t_1^{\text{exp}}) - (t_2^{\text{meas}} - t_2^{\text{exp}}))^2}{\sigma_{t_1}^2 + \sigma_{t_2}^2 + \sigma_{\beta_2}^2 + \sigma_{\beta_1}^2 + \sigma_{l_1}^2 + \sigma_{l_2}^2}. \quad (4.4)$$

$\sigma_{t_i}$  is the uncertainty on the measured time-of-flight.  $\sigma_{\beta_i}$  and  $\sigma_{l_i}$  are the uncertainties on the expected time-of-flight brought by the uncertainty on particle energies and track lenghts, respectively. The denominator square root corresponds to the total uncertainty, whose sigma value is simulated as zero and dergraded afterwards.

In the official SuperNEMO reconstruction pipeline,  $\sigma_l = \sigma_{l_1} = \sigma_{l_2} = 70$  ps for electron particles. As we simulated perfect calorimeters, we check that this

parameter is correctly evaluated in order to implement it in our own off-line Root code pipeline.

### Optimisation of $\sigma_l$

One way to examine if  $\sigma_l$  is well-evaluated is to look at the flatness of the internal probability distribution for  $0\nu\beta\beta$  events in the  $2e$  topology, for which a flat distribution is expected. Indeed, the slope of this distribution provides pertinent information to check the estimation of uncertainties. The flatter the distribution, the more correctly uncertainties are estimated.

Therefore, for this optimisation, we use  $2e$  topologies of signal simulations inside the source foils. Discret values of  $\sigma_l$  running from 0.01 to 0.1 ns are used to compute the internal probability distributions of these events. For each distribution, a linear fit is performed on the reduced range  $P_{int} \in [0.1; 1]$  in order to avoid the peak at low internal probabilities. The *flatness parameter*  $a_F$  is defined as the slope parameter of the linear fit. The optimisation then consists in finding the value of  $\sigma_l$  for which the parameter  $a_F$  is cancelled, which corresponds to the best estimate for  $\sigma_l$ .

In Fig. 4.3 is given the slope  $a_F$  as a function of  $\sigma_l$ . For  $\sigma_l = 70$  ps,  $a_F > 0$ ,

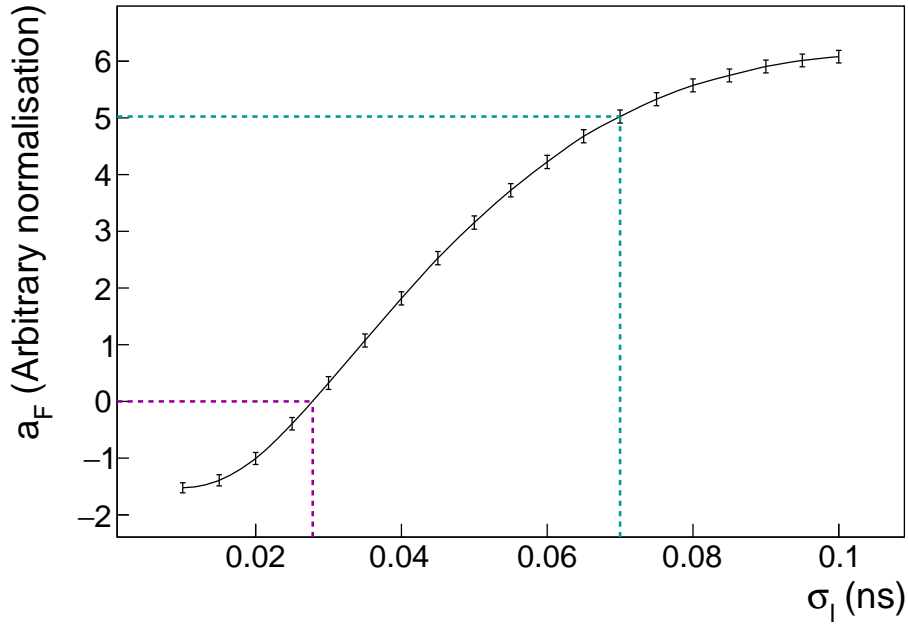


Figure 4.3: Slope  $a_F$  as a function of the time uncertainty due to the reconstructed track length  $\sigma_l$ . The former value used in the SuperNEMO reconstruction pipeline is pointed out by blue dashed lines. The value kept for  $\sigma_l$  is the one for which  $a_F = 0$ ,  $\sigma_l = 27.8 \pm 0.8$  ps, showed by purple dashed lines.  $P_{int}$  is calculated for  $0\nu\beta\beta$  decays simulated inside the source foil, with first order cut-offs applied.

revealing an overestimation of uncertainties in the computation of the internal  $\chi^2$  in the SuperNEMO reconstruction pipeline, at the Particle Identification module

level. The optimised value, kept for the further analysis, is  $\sigma_l = 27.8 \pm 0.8$  ps. In Fig. 4.4 is displayed the internal probability distributions for these two values of the  $\sigma_l$  parameter,  $\sigma_l = 70$  ps and  $\sigma_l = 27.8$  ps.

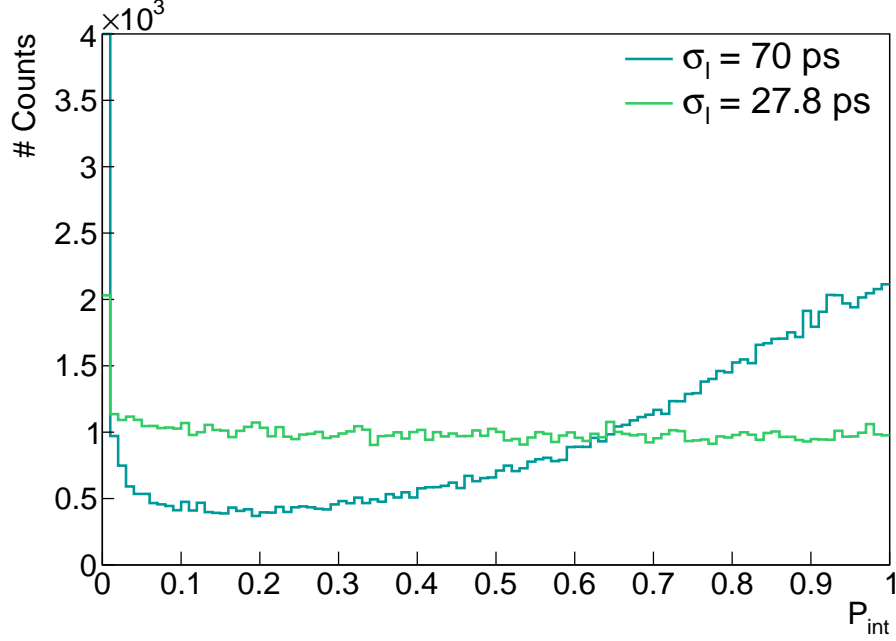


Figure 4.4: Internal probability distributions for  $\sigma_l = 70$  ps (blue) and  $\sigma_l = 27.8$  ps (green).  $P_{int}$  is calculated for  $0\nu\beta\beta$  decays simulated inside the source foil, with first order cut-offs applied.

Let us notice that normally  $\sigma_l$  should depend on the track length as well as the energy, especially as multiple scatterings in the tracker have a more notable impact for low energy electrons. A more complete analysis would then compare the simulated track lengths with the reconstructed ones, for different energy simulated sets of mono-kinetic electrons, to evaluate this dependence. Nevertheless, our optimisation is good enough for the current analysis. Discussions are in progress to modify this parameter in the SuperNEMO software.

The internal probability is principally designed to reject non-simultaneous events coming from the source foils. Therefore, it is extremely effective in rejecting  $^{222}\text{Rn}$  events produced far from the source foils. Even if it is less, this criterion is also effective in rejecting  $^{208}\text{Tl}$  events due to the metastable state of the 2.615 MeV- $\gamma$ . But to describe even better these internal conversion events we would set up a new probability law expressing the hypothesis that a given event is from a  $\beta$ +IC delayed  $^{208}\text{Tl}$  disintegration.

#### 4.4.2 The exponential probability for $^{208}\text{Tl}$ events

According to the disintegration scheme of the  $^{208}\text{Tl}$  isotope (Fig. 4.1), there is an 81 % probability of passing through the 294 ps metastable level. After that, to reach the ground state of  $^{208}\text{Pb}$ , the excited nucleus has 100% of probability to decay through the 2.615 MeV energy level. At this occasion, in 0.246% of cases



(Tab. 4.2), one of the orbital electrons is ejected from the atom following the internal conversion process. To summarise, for 0.20 % of the total  $^{208}\text{Tl}$  decays, a  $\beta$  particle is emitted, and a delayed orbital electron is ejected through internal conversion of the 2.6 MeV- $\gamma$ . Furthermore,  $X\%$  of the events with an energy sum greater than 2.7 MeV (the ROI low bound) are from delayed internal conversion decays and could be harmful for the  $0\nu\beta\beta$  search. We aim to use this delayed electron to discriminate  $^{208}\text{Tl}$  internal background from the  $0\nu\beta\beta$  signal.

- relire cette partie quand les sinus sont finies

#### 4.4.2.1 Probability density function

For a given detected  $2e$  topology, we define the  $\Delta t^{meas}$  parameter as

$$\Delta t^{meas} = t_1^{meas} - t_2^{meas}, \quad (4.5)$$

where  $t_1^{meas}$  and  $t_2^{meas}$  are the two measured time-of-flights, where  $t_2$  stands for the electron of lowest energy, and  $t_1$  for the one of highest energy. If this  $2e$  topology corresponds to a delayed  $^{208}\text{Tl}$  event, then the electron of lowest energy is supposed to be a  $\beta$  particle and the one of highest energy an electron coming from an internal conversion, delayed in average of 294 ps. Assuming an ideal calorimeter perfectly measuring time-of-flights and energies, the  $\Delta t$  distribution for such delayed events would be a decreasing exponential, with the decay parameter  $\tau = 294$  ps. However, in actual conditions, this exponential is degraded by the uncertainties on time-of-flight measurements detailed in Eq. (4.4). These are embedded by a Gaussian distribution centred around  $\mu = 0$  ps with a given width  $\sigma$ . Therefore, to each  $2e$  topology is associated a probability density function which is the convolution between an exponential and a Gaussian distribution, written down as  $(E \otimes G)_{\tau,\mu,\sigma}(\Delta t)$ . The corresponding value of  $\Delta t^{meas}$  is then found somewhere on this distribution, and will serve us to define the so-called *exponential probability*,  $P_{exp}(\Delta t^{meas})$ , which is the probability that this event comes from a  $\beta$ +IC delayed decay.

- Du coup mettre une distribution de ces ev sur l'exponentielle quand les sinus seront finies

#### 4.4.2.2 Exponential probability

We wish to define this probability following the same principle as for the internal probability, for comparison purposes. Therefore, we would obtain the maximal value  $P_{exp} = 1$  when the value of  $\Delta t$  is the most favourable, i.e. when  $\Delta t$  is of the order of the mean of the  $(E \otimes G)_{\tau,\mu,\sigma}(\Delta t)$  distribution. On the other hand, minimal values for  $P_{exp}$  would be reached for unfavourable values of  $\Delta t$ , so  $P_{exp} \xrightarrow{|\Delta t| \rightarrow +\infty} 0$ .

To do so, the  $(E \otimes G)_{\tau,\mu,\sigma}(\Delta t)$  distribution is normalised and the exponential probability is defined as

$$P_{exp}(\Delta t^{meas}) = \int_{-\infty}^{\Delta t^{meas}} (E \otimes G)_{\tau,\mu,\sigma}(t) dt + \int_{\Delta t_{sym}^{meas}}^{-\infty} (E \otimes G)_{\tau,\mu,\sigma}(t) dt, \quad (4.6)$$

where  $\Delta t_{sym}^{meas}$  is defined according to  $\Delta t^{meas}$  of which a graphical representation is given in Fig. 4.5. In this example the distribution corresponds to  $(E \otimes G)_{\tau,\mu,\sigma}(\Delta t)$

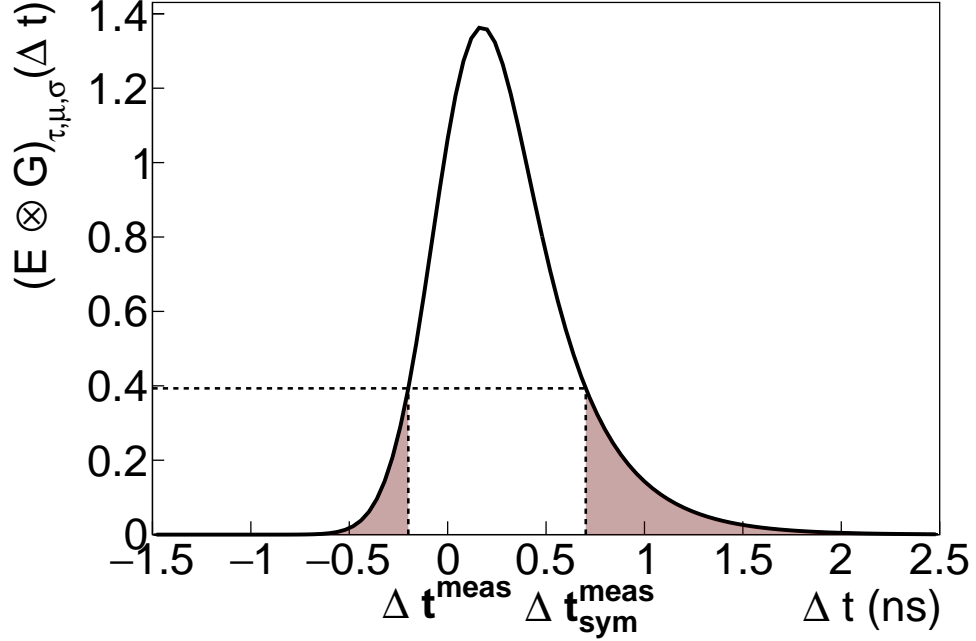


Figure 4.5: Normalised convolution distribution  $(E \otimes G)_{\tau,\mu,\sigma}(\Delta t)$ . The parameters are  $\tau = 294$  ps,  $\mu = 0$  ps and  $\sigma = \sigma_{tot}$ , computed with  $\sigma_l = 27.8$  ps and  $\sigma_t = 200$  ps.

with  $\tau = 294$  ps and  $\mu = 0$  ps and the total time uncertainty is calculated taking  $\sigma_l = 27.8$  ps and  $\sigma_t = 200$  ps. The two integrals whose sum is given in the Eq. (4.6) are represented by two red-coloured areas. As explained, each probability density function is defined for a single 2-electrons event. Therefore, it depends on the value of the measured energies for the two particles detected. In the given example, we considered two particles interacting inside the calorimeter with an energy of 1 MeV each.

In fig. 4.6 are presented exponential probability distributions for  $2e$  topologies selected of  $^{208}\text{Tl}$  and  $0\nu\beta\beta$  simulations inside the source foils. As expected, the distribution is flat, since this probability was defined in the same way as the internal probability.

Now analysis tools are defined, the following sections focus on the event selections using them, the way to optimise them and their influence on the final detector sensitivity.

## 4.5 Event selection

Now the exponential probability tool has been defined, the aim of this analysis is to set up events selections focusing on delayed  $^{208}\text{Tl}$  events rejection. Basic cut-offs are described, and compared with a more elaborated selection using these two probabilities. The influence of the uncertainty  $\sigma_t$  on time measurement is discussed at the end of the section.

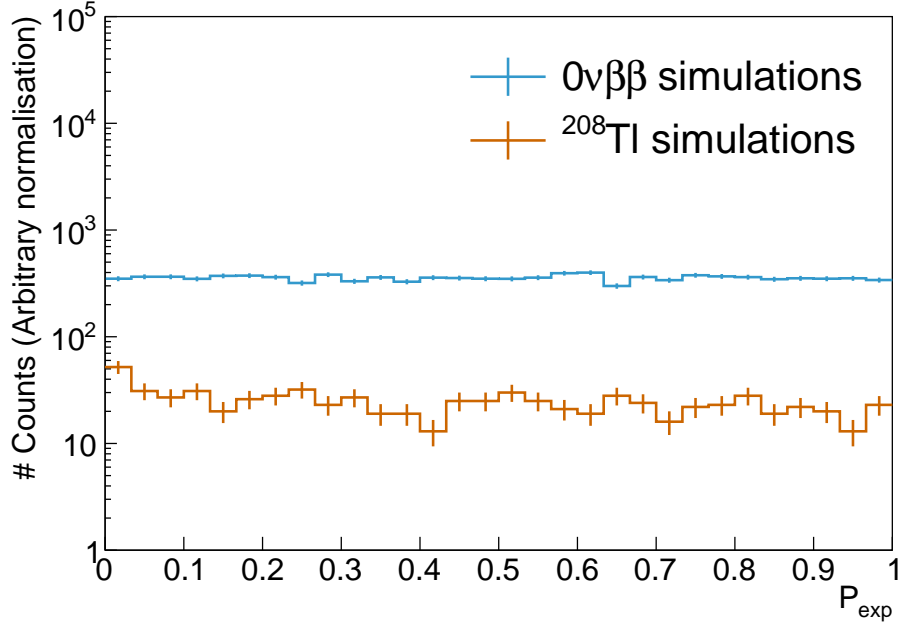


Figure 4.6: Exponential probability distribution for  $^{208}\text{Tl}$  (orange) and  $0\nu\beta\beta$  simulations (blue), for  $2e$  topologies with an electron energy sum greater than 2.7 MeV (discussed in Sec. 4.5).  $\sigma_t = 200$  ps,  $\sigma_l = 27.8$  ps.

#### 4.5.1 Energy selection

Based on the conclusions given in the previous chapter, the lower bound of the region of interest optimising the search of  $0\nu\beta\beta$  decay stands at the electron energy sum of 2.7 MeV. From this energy,  $2e$  topologies for  $^{208}\text{Tl}$  are mainly populated by  $\beta$  decays followed by the internal conversion of the 2.615 MeV  $\gamma$ -ray. In the following, we therefore focus only on events with a sum in energy of the two detected electrons greater than 2.7 MeV.

#### 4.5.2 Time-of-flight cut-off

Before using the two internal and exponential probabilities, a simple cut-off using the electron time-of-flight is explored. Indeed, we are especially focused on rejecting the internal  $^{208}\text{Tl}$  events for which the successive  $\gamma$ -rays emissions went through the 294 ps half-life metastable state. For these decays, we are expecting the particle of highest energy to be delayed compared with the one of lowest energy. Each term in Eq. 4.5 corresponds to what it took for a particle to travel from the source to the calorimeter and depends on the time it spent in the source after emission, as well as how long it took to cross the tracker. In order to remove from  $\Delta t^{\text{meas}}$  the dependency on travel time in the tracker, we define the corrected time difference as

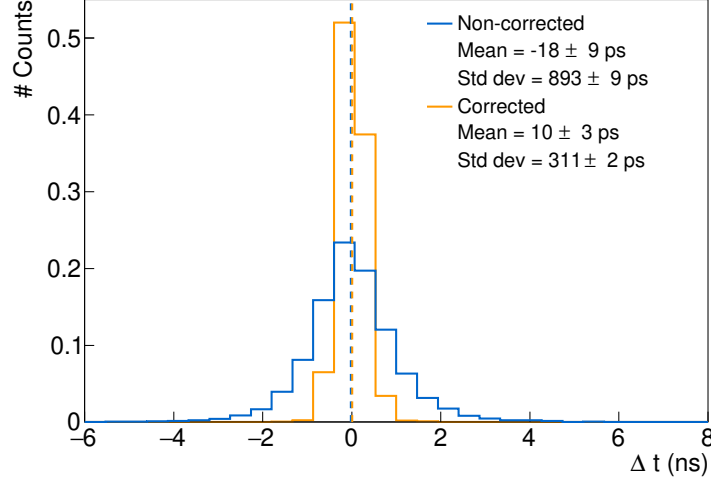
$$\Delta t^{\text{corr}} = t_1^{\text{corr}} - t_2^{\text{corr}} \quad (4.7)$$

$$= (t_1^{\text{meas}} - t_1^{\text{exp}}) - (t_2^{\text{meas}} - t_2^{\text{exp}}), \quad (4.8)$$

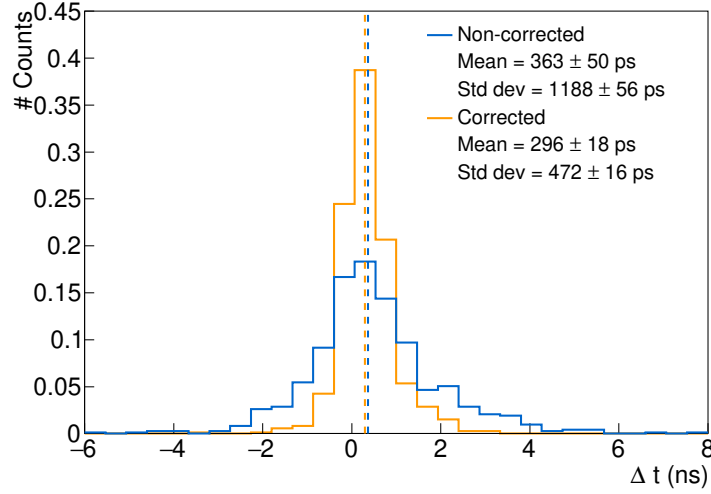
#### 4. IMPROVEMENT OF THE INTERNAL THALLIUM-208 BACKGROUND REJECTION

where  $t_i^{\text{corr}}$  are the corrected time-of-flights and  $t_i^{\text{exp}}$  the expected ones calculated with the particle energy and track length (Eq. 2.2).

The two distributions  $\Delta t^{\text{meas}}$  and  $\Delta t^{\text{corr}}$  are presented in Fig. 4.7, for  $0\nu\beta\beta$  and  $^{208}\text{Tl}$  simulations inside the source foils. For  $0\nu\beta\beta$  simulations, the  $\Delta t^{\text{corr}}$



(a)  $0\nu\beta\beta$  simulations.



(b)  $^{208}\text{Tl}$  simulations.

Figure 4.7: Corrected (orange) and non-corrected (blue) time-of-flight difference between the two electrons. (a)  $0\nu\beta\beta$  simulations inside the source foils. (b)  $^{208}\text{Tl}$  simulations inside the source foils. The first-order selections have been applied. The two distributions are normalised.  $\sigma_t = 200$  ps and  $\sigma_l = 27.8$  ps.

distribution is centred around zero, as the two electrons are emitted simultaneously inside the source. Then, the correction on time difference only lowers the standard deviation of the distribution. For  $^{208}\text{Tl}$  simulations, the mean of the distribution is slightly shifted towards positive values. Once corrected by the expected times, the mean difference between the two electrons time-of-flights stands at  $296 \pm 18$  ps. This is a direct consequence of the existence of  $\beta+\text{IC}$  delayed events, for which

the particle of highest energy is expected to hit a calorimeter block at a time  $t_1^{\text{corr}} > t_2^{\text{corr}}$ . The set up calorimeter time uncertainty at 200 ps allows to be sensitive to this decay as the mean of the distribution is near 294 ps. Therefore, a simple way of rejecting the  $^{208}\text{Tl}$  delayed events is to consider the sign of  $\Delta t^{\text{corr}}$  and to reject events for which  $\Delta t^{\text{corr}} > 0$ .

By applying this selection on  $2e$  topologies of  $0\nu\beta\beta$  and  $^{208}\text{Tl}$  simulations for which  $E > 2.7$  MeV, we are able to reject 76 % of  $^{208}\text{Tl}$  while selecting 49 % of the  $0\nu\beta\beta$  ( $\sigma_t = 200$  ps). The 49% of selected signal events is expected as the corresponding  $\Delta t^{\text{corr}}$  distribution is symmetrical, unlike the one for  $^{208}\text{Tl}$  events. Although we manage to reject a significant fraction of Thallium events, the impact of this cut is too high on  $0\nu\beta\beta$  events. Moreover, the uncertainties on time-of-flights are not taken into account in the rejection criterion. Later in this chapter we consider different levels for this selection and optimise them according to the  $\sigma_t$  value set up.

### 4.5.3 Probability cut-off

At this level it is interesting to consider the internal and exponential probabilities to describe  $2e$  topologies and attempt to obtain a higher background rejection. They seem to be better tools notably because, unlike the  $\Delta t^{\text{corr}}$  rejection criterion, they do take into account the time-of-flight uncertainties. The first one was already used in Chapter 3, and is a widely-used tool to reject non-internal events. The second was designed specifically for this analysis to identify delayed  $^{208}\text{Tl}$  events, and also depends on the time of flight resolution through the convolution with a Gaussian function.

The idea in this section is to reject  $^{208}\text{Tl}$  events taking into account their two values of internal and exponential probabilities. Then it is interesting to represent them with a two-dimensional binned histogram of  $P_{\text{exp}}$  as a function of  $P_{\text{int}}$ , as done in Fig. 4.8. In this particular example, we picture the variations of  $P_{\text{int}}$  and  $P_{\text{exp}}$  applying  $\sigma_t = 200$  ps. We clearly distinguish three event populations in this histogram. In order to better understand these variations, we give in Fig. 4.9 three examples of  $(E \otimes G)_{\tau,\mu,\sigma}(\Delta t)$  distributions, each of them illustrating one of the three zones.

1.  $P_{\text{int}} \in [0; 1]$  and  $P_{\text{exp}} \in [0; 0.65]$ , with  $P_{\text{int}} > P_{\text{exp}}$  (Fig. 4.9a):  
This region corresponds to events for which  $\Delta t^{\text{corr}} < 0$ . As the internal  $\chi_{\text{int}}^2$  distribution is symmetrical, such events can have a value of  $P_{\text{int}}$  varying from 0 to 1. Small values of  $P_{\text{int}}$  correspond to events with a large  $\Delta t^{\text{corr}}$  in absolute value. Conversely, the exponential distribution is not centred in zero. Therefore, if we limit to events for which the time difference is negative, we reach an upper bound for the value of the integral (0.65 in that case). This bound directly depends on the variations of the exponential distribution, therefore on the  $\sigma_t$  value applied.
2.  $P_{\text{int}} \in [0; 0.65]$  and  $P_{\text{exp}} \in [0; 1]$ , with  $P_{\text{exp}} > P_{\text{int}}$  (Fig. 4.9b):  
These events have positive values for  $\Delta t^{\text{corr}}$ , beyond the  $(E \otimes G)_{\tau,\mu,\sigma}(\Delta t)$  distribution maximum. The smaller the value of  $P_{\text{int}}$ , the lower the

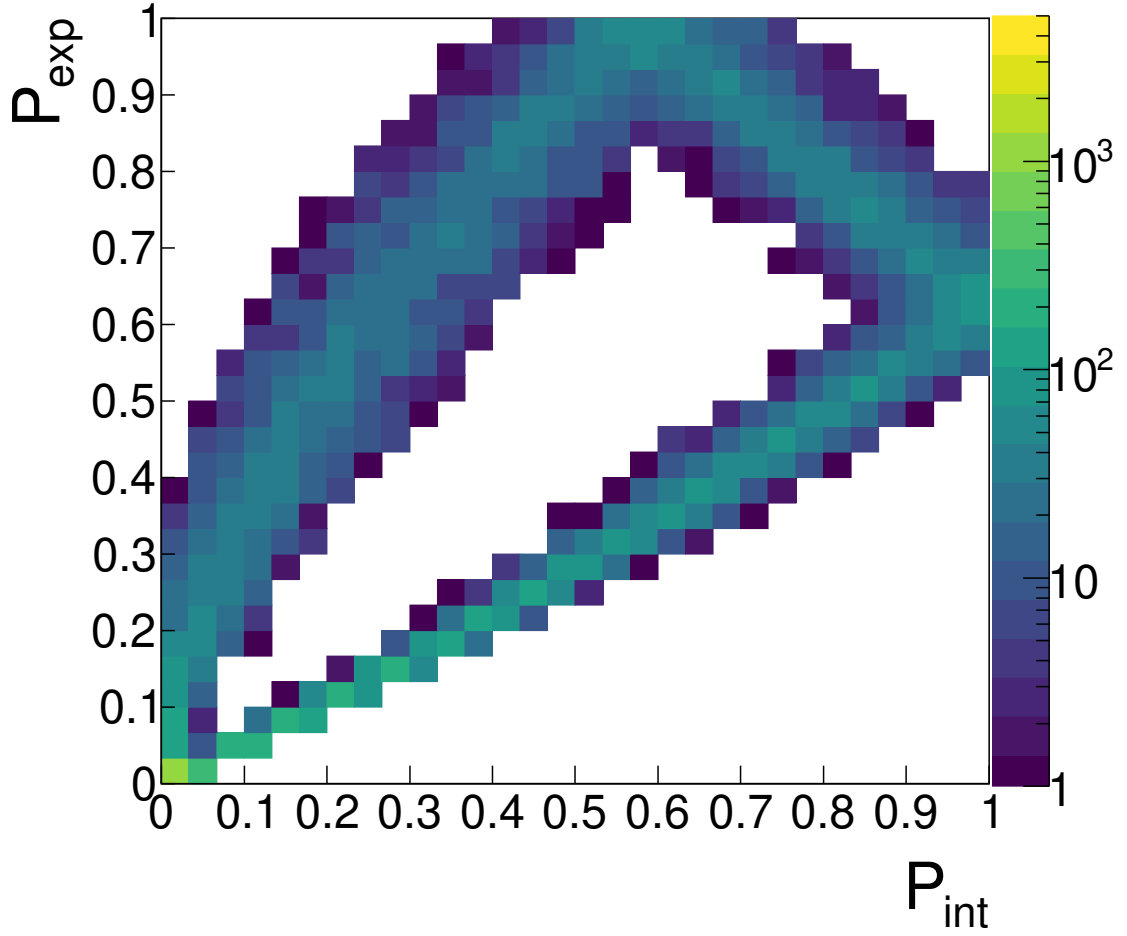


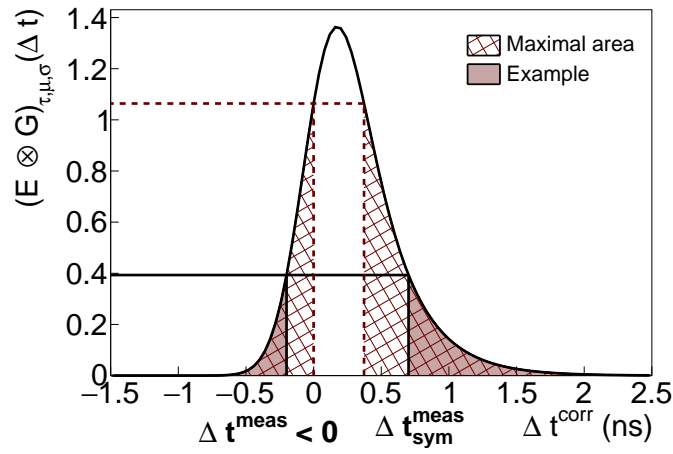
Figure 4.8: Two-dimensional histogram showing the  $P_{exp}$  variations as a function of  $P_{int}$  for  $^{208}\text{Tl}$  2e topologies.  $\sigma_t = 200$  ps and  $\sigma_l = 27.8$  ps.

probability that both particles were emitted at the same time into the source. Besides, for values of  $\Delta t^{\text{corr}}$  highly positives, the value of the exponential probability can reach high values, up to 1. The larger the value of  $\Delta t^{\text{corr}}$  in positives, the smaller the value of  $P_{exp}$ .

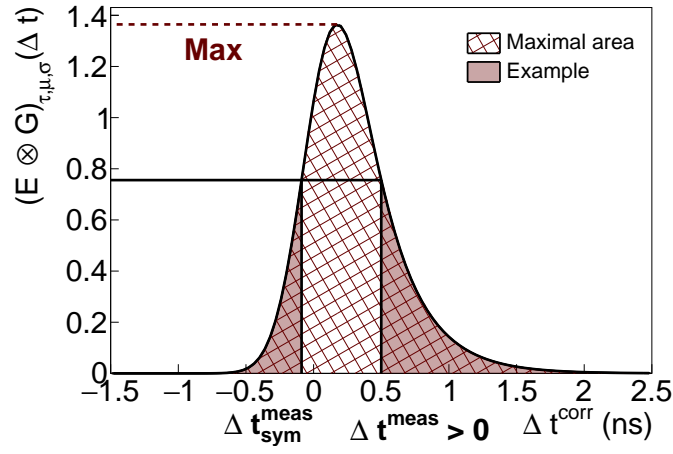
3.  $P_{int} \in [0.65; 1]$  and  $P_{exp} \in [0.65; 1]$  (Fig. 4.9c):

This region is also populated by events for which  $\Delta t^{\text{corr}} > 0$ . Unlike the previous case, these events have small  $\Delta t^{\text{corr}}$  values, meaning below the maximum of the exponential distribution. Also, these events have high internal probability values, as the probability that these two particles were emitted simultaneously is high. In the same way as the first bullet, the value of  $P_{exp}$  is bounded: the lower bound corresponds to the value of the integral when  $\Delta t^{\text{corr}} = 0$  (here 0.65). Once again, this bound is deeply related to the value considered for  $\sigma_t$ . The exponential probability can be equal to 1 when  $\Delta t^{\text{corr}}$  reaches the maximum of the exponential distribution.

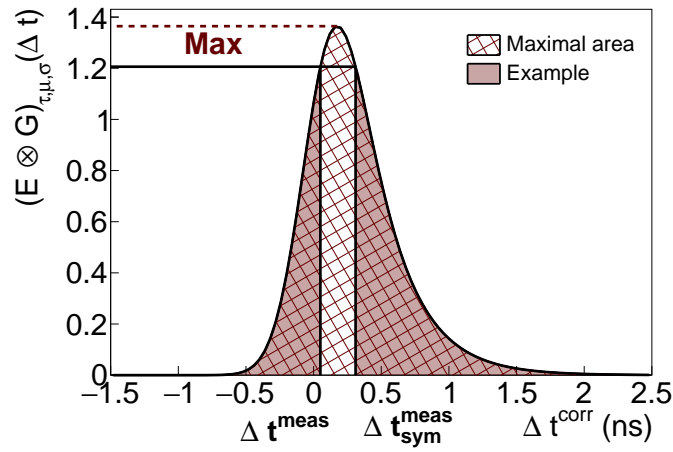
As discussed, the exponential probability quantifies the likelihood that two



(a)




(b)



(c)

Figure 4.9:  $(E \otimes G)_{\tau,\mu,\sigma}(\Delta t)$  distributions describing the three areas observed in Fig. 4.8. (a)  $\Delta t^{\text{corr}} \in ]-\infty; 0]$ . (b)  $\Delta t^{\text{corr}} \in ]\Delta t_{\text{max}}; +\infty]$ . (c)  $\Delta t^{\text{corr}} \in ]0; \Delta t_{\text{max}}]$ .



particles were emitted with a delay corresponding to the radioactive exponential decay with  $\tau = 294$  ps, taking into account the time of flight resolution. Therefore, we are interested in rejecting events for which values of  $P_{exp}$  are high compared with the  $P_{int}$  values. In that case, a simple selection allowing to discriminate signal  $0\nu\beta\beta$  from delayed  $^{208}\text{Tl}$  event consists in rejecting  $2e$  topologies for which  $P_{exp} > P_{int}$  (this cut-off is pictured in Fig. 4.8 by a plain black line). With the previous explanation, we understand  such a cut is strongly linked to the cut on  $\Delta t^{\text{corr}}$  presented in the previous sub-section.

We would like to refine the selection made on the events using the two probabilities. Regarding the biplot presented in Fig. 4.8, the goal is to reject events located in the area 3 and a part of the events located in area 2. Therefore, a more adapted cut-off is to reject events for which  $P_{exp} > 0.65$ . For this selection and  $\sigma_t = 200$  ps, we reject 20% of  $^{208}\text{Tl}$  and keep 84% of  $0\nu\beta\beta$  events. The proportion of signal events kept with this selection is satisfying. Nevertheless the efficiency of  $^{208}\text{Tl}$  rejection is almost 4 times lower than for the time-of-flight selection presented in Sec. 4.5.2.



#### 4.5.4 Influence of the calorimeter time resolution

We study in this subsection the influence of the calorimeter timing resolution on event selections, using the cut-offs presented above. We consider values for  $\sigma_t$  in the  $[0 - 400]$  ps range.

In Sec. 4.5.2 we presented rejection efficiencies for a  $\Delta t > 0$  ps selection, with  $\sigma_t = 200$  ps. In Fig. 4.10 is presented the  $0\nu\beta\beta$  selection efficiency with the rejection efficiency of  $^{208}\text{Tl}$ , for values of  $\sigma_t$  running from the ideal 0 ps, to 400 ps. Each point corresponds to a  $\Delta t$  level applied on the selected  $2e$  topologies, from  $\Delta t > 0$  to  $\Delta t > 650$  ps. For  $\Delta t > 0$  and  $\sigma_t = 200$  ps, we get back to the result given previously. Nevertheless, for this time uncertainty, an optimised value for the  $\Delta t$  cut level, called *maximum efficiency point*, is found at  $\Delta t > 250$  ps as it optimises the signal selection and  $^{208}\text{Tl}$   background rejection efficiencies. Such a point can be found for each of the five  $\sigma_t$  values presented. The more precisely the time-of-flight is measured in the calorimeter, the better this point is determined . Indeed, the worse this resolution is, the more linear the distribution tends to be, and therefore the more difficult it is to discriminate delayed events from those emitted simultaneously such as those of  $0\nu\beta\beta$ . Especially, for an ideal calorimeter where the timing measurement would be perfect, we could reach 80% of  $^{208}\text{Tl}$  rejection, while keeping 90% of signal events.

As discussed, the variations of  $P_{int}$  and  $P_{exp}$  are binded to the value of  $\sigma_t$ , thus the levels applied on  $P_{int}$  and  $P_{exp}$  must be adapted to match these variations. Eight  $P_{int}/P_{exp}$  biplots are given in Fig. 4.11, for  $\sigma_t = 0, 100, 300$  and 400 ps both for  $0\nu\beta\beta$  and  $^{208}\text{Tl}$   $2e$  selected topologies (the  $\sigma_t = 200$  ps case is already given in Fig. 4.8). Depending on  $\sigma_t$ , the area to be rejected moves towards higher values of  $P_{int}$ . Taking this into consideration, optimised values for  $P_{int}$  have been set up, summarised in Tab. 4.3. To find an optimal value of  $P_{exp}$  to be applied, several cut-offs are set up from  $P_{exp} > 0$  to 0.95, and associated with the  $P_{int}$  cut-offs presented in the previous table, in order to reject the required area. Following the work done



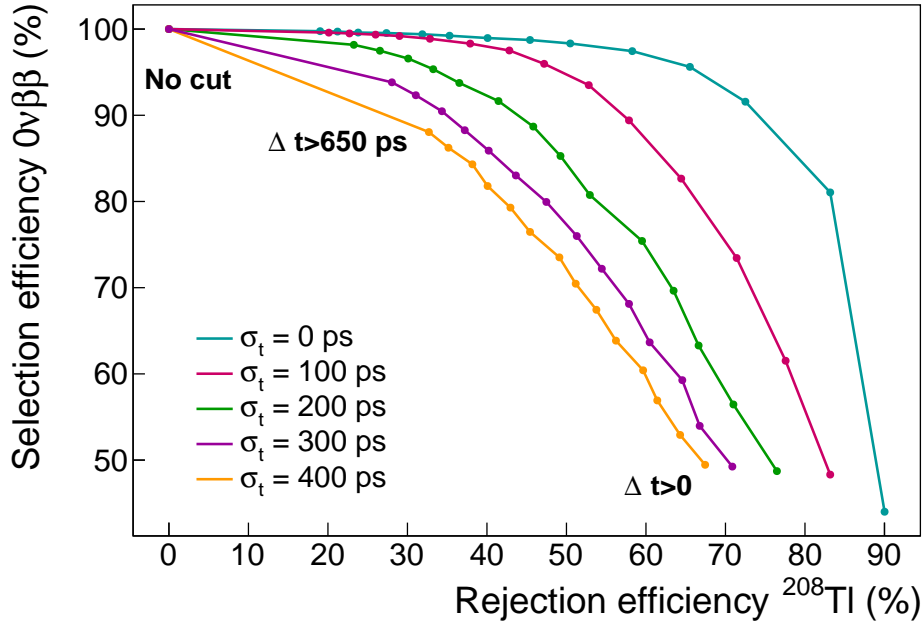


Figure 4.10:  $0\nu\beta\beta$  selection efficiency as a function of  $^{208}\text{Tl}$  rejection. Each curve corresponds to a given value of  $\sigma_t$  from 0 to 400 ps. Each data point corresponds to a minimum value for  $\Delta t$  applied on selected 2 topologies from 0 to 650 ps. the optimised value of  $\sigma_l = 27.8$  ps is applied.

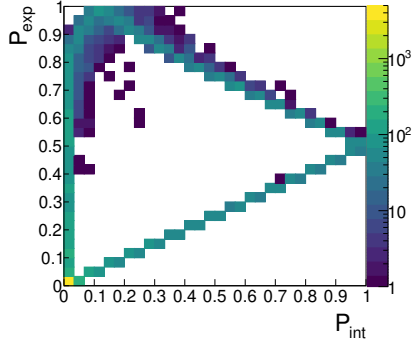
$\sigma_t$ (ps)	0	100	200	300	400
$P_{int}$ cut-off	[0.05 - 0.3]	[0.25 - 0.6]	[0.4 - 0.7]	[0.5 - 0.8]	[0.55 - 0.85]

Table 4.3: Range of  $P_{int}$  for which events are rejected. An additional cut-off with  $P_{int} < 0.01$  and  $P_{exp} < 0.01$  is also applied.

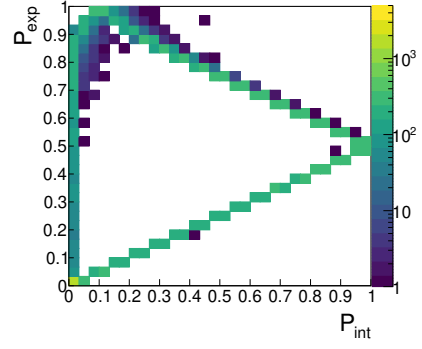
for the  $\Delta t$  cut-off, results are presented in Fig. 4.12 on an efficiency selection diagram. The calorimeter timing measurement has a great influence, especially on  $^{208}\text{Tl}$  events rejection. Evolution of selection efficiencies for  $\sigma_t < 200$  ps are very similar, reaching a plateau for  $\sim P_{exp} > 0.25$  allowing to reject 2% of  $^{208}\text{Tl}$  while keeping 85% of  $0\nu\beta\beta$ . Below  $\sigma = 100$  ps the background rejection is improved despite a loss in signal selection efficiency, up to reaching  $\sim 45\%$  of  $^{208}\text{Tl}$  rejection and  $\sim 80\%$  signal selection for an ideal calorimeter. The plateau is reached at  $P_{exp} > 0.2$  for  $\sigma_t = 100$  ps and  $P_{exp} > 0.15$  for  $\sigma_t = 0$  ps.

A better Thallium rejection can be obtained with the simple selection on time-of-flights, but the probability one has the main advantage to be more accurate as it takes into account the calorimeter time measurement uncertainties. Moreover, even if variations of selection/rejection of this diagram are not as pronounced as for the  $\Delta t$  cut-off, a strong assumption can be made: the more we are precise on time-of-flight measurements, the more we are able to reject  $^{208}\text{Tl}$  events while keeping a satisfying part of signal. During the calorimeter R&D, a great effort has been made to improve the optical modules energy resolution compared to NEMO-3, notably because it allows to have a better background rejection, and

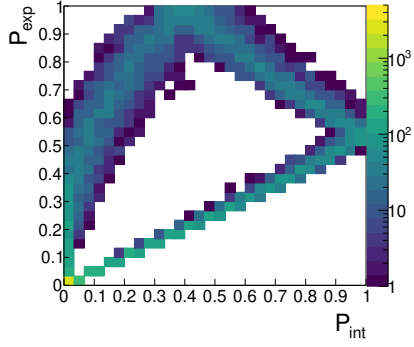
#### 4. IMPROVEMENT OF THE INTERNAL THALLIUM-208 BACKGROUND REJECTION



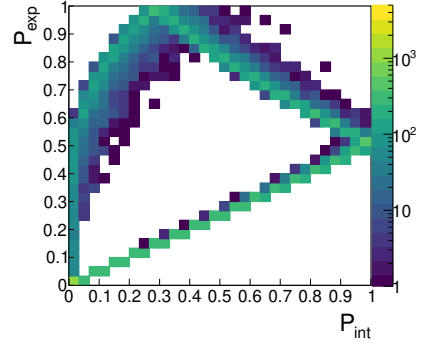
(a)  $^{208}\text{Tl}$  simulations,  $\sigma_t = 0$  ps.



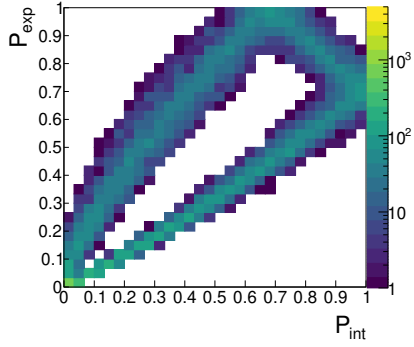
(b)  $0\nu\beta\beta$  simulations,  $\sigma_t = 0$  ps.



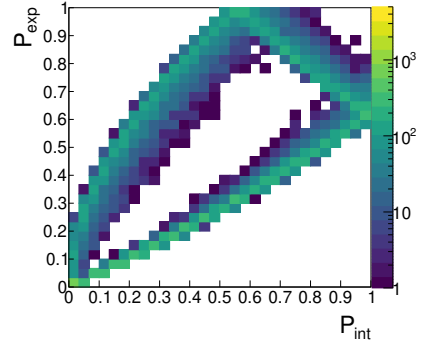
(c)  $^{208}\text{Tl}$  simulations,  $\sigma_t = 100$  ps.



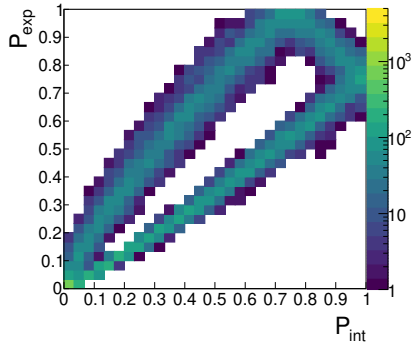
(d)  $0\nu\beta\beta$  simulations,  $\sigma_t = 100$  ps.



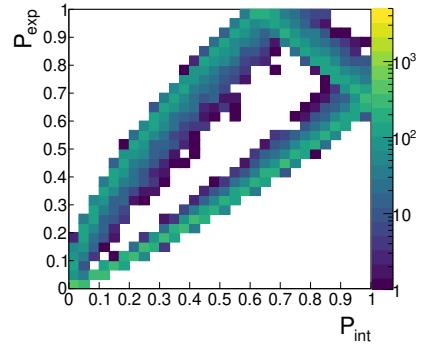
(e)  $^{208}\text{Tl}$  simulations,  $\sigma_t = 300$  ps.



(f)  $0\nu\beta\beta$  simulations,  $\sigma_t = 300$  ps.



(g)  $^{208}\text{Tl}$  simulations,  $\sigma_t = 400$  ps.



(h)  $0\nu\beta\beta$  simulations,  $\sigma_t = 400$  ps.

Figure 4.11:  $P_{int}/P_{exp}$  biplots for different  $\sigma_t$  values for  $^{208}\text{Tl}$  and  $0\nu\beta\beta$  simulations.

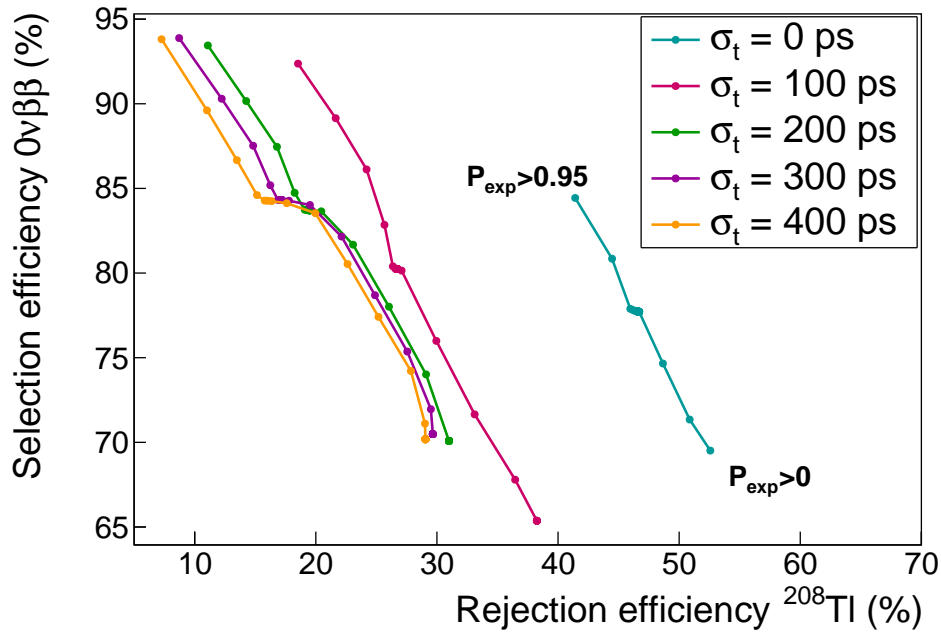


Figure 4.12:  $0\nu\beta\beta$  selection efficiency as a function of  $^{208}\text{Tl}$  rejection. Each data point corresponds to a given value of  $\sigma_t$ , decrementing in 50 ps steps. First order selections applied on  $0\nu\beta\beta$  and  $^{208}\text{Tl}$  simulations.  $\sigma_l = 27.8$  ps.

thus to decrease its contribution to the  $0\nu\beta\beta$  search. Finally, in view of these results, a good timing precision in calorimeter blocks is also important when it concerns background rejection, and especially the identification of  $\beta$ +IC delayed  $^{208}\text{Tl}$  decays. Nevertheless, to give a final conclusion on the usefulness of the  $\Delta t$  and probability cut-offs, one have to study its impact on the final sensitivity of the detector, which is dealt with in the next section.

## 4.6 Impact of $^{208}\text{Tl}$ rejection on the experiment's sensitivity

Reprendre l'analyse de sensibilité faite avec Axel en rajoutant les cuts  $P_{\text{int}}/P_{\text{exp}}$  et  $\Delta t$  pour le final detector

- on regarde les autres isotopes: Tableau eff
- cut efficiencies ( $\Delta t$  et proba) on other backgrounds
- Se servir des résultats de  $\sigma_t$  trouvés au chap. ??
- Mais dire que ces sigmas peuvent être améliorés
- donc présenter l'évolution des résultats (efficacité de réjection et sensibilité) sur la réjection en fonction de la valeur de  $\sigma_t$ , à faire varier dans un certain range.

- Tu pourrais avec une figure à 2D où tu montres l'efficacité relative  $0_{nu}$  (égale à 100% avant cette coupure temporelle) en fonction de la réjection du Tl208 -> cela donne une courbe que tu parcoures et tu cherches à optimiser ton point de fonctionnement.
- Peut-être que quand tu commenteras la courbe tu pourras insister sur le rôle très important de l'amélioration de  $\sigma_t$ , en donnant des chiffres pour une efficacité  $0_{nu}$  fixée (par exemple à 95%), voir quelle serait la réjection du Tl208 pour  $\sigma_t = 400$  ps, 200ps, 100 ps.

## 4.7 Conclusion

During this chapter we have defined or specified analysis tools adapted to the rejection of background. In particular, a so-called exponential probability law has been defined to describe the internal events of delayed Thallium. Although the cut-off based on the electron time-of-flight is very satisfactory for rejecting this last background, the associated cut-off in internal and exponential probability makes it possible to be more precise since it takes into account the errors made on the time-of-flight measurements in the calorimeter. These rejection could be tested on site using a  $^{232}\text{U}$  calibration source, a parent of  $^{208}\text{Tl}$  nucleus, inside the calorimeter to enhance the Thallium disintegration rate detected.

We have determined the influence the time resolution has on the various defined cut-off efficiencies. The worse this resolution is, the more difficult it is to discriminate thallium events from signal events. Improving the time resolution of the calorimeter was not a direct purpose of the R&D programme, however it has benefited from the high light output achieved to meet the energy resolution goals. The time resolution of the optical modules has been monitored at every stage of the R&D programme but remains to be precisely determined. This is precisely the purpose of the next chapter, which describes how we determined the time resolution of the optical modules of the demonstrator calorimeter with a  $^{60}\text{Co}$  source.



---

## Bibliography

- [1] M. Agostini et al. Probing majorana neutrinos with double- $\beta$  decay. *Science* 365, 1445, 2019.
- [2] S.I. Alvis et al. Search for neutrinoless double-beta decay in  $^{76}\text{Ge}$  with 26 kg-yr of exposure from the majorana demonstrator. *Phys. Rev. C*, 100, 2019.
- [3] O. Azzolini et al. First result on the neutrinoless double- $\beta$  decay of  $^{82}\text{Se}$  with cupid-0. *Phys. Rev. Lett.*, 120:232502, Jun 2018.
- [4] C. Alduino et al. First results from cuore: A search for lepton number violation via  $0\nu\beta\beta$  decay of  $^{130}\text{Te}$ . *Phys. Rev. Lett.*, 120:132501, Mar 2018.
- [5] J. B. Albert et al. Search for neutrinoless double-beta decay with the upgraded exo-200 detector. *Phys. Rev. Lett.*, 120:072701, Feb 2018.
- [6] A. Gando et al. Search for majorana neutrinos near the inverted mass hierarchy region with kamland-zen. *Phys. Rev. Lett.*, 117:082503, Aug 2016.
- [7] Chopra A. C0 commissioning results. Internal presentation, 2015.
- [8] Cerna C. Tracker review conclusions. Internal presentation, 2014.
- [9] S. Clavez. *Development of reconstruction tools and sensitivity of the SuperNEMO demonstrator*. PhD thesis, Université Paris Sud, 2017.
- [10] Garrido X. Bongrand M. Hamamatsu 8" pmt test in magnetic shield. Internal presentation, 2014.
- [11] Loaiza P. Source foils measurement with bipo. Internal presentation, 2017.
- [12] Perrot F. Radiopurity measurements for 8" pmts and preliminary budget for the sn demonstrator. Internal presentation, 2017.
- [13] et al Arnold R. Technical design and performance of the nemo3 detector. *Nucl. Instrum. Meth. A*, pages 79–122, 2005.
- [14] Xin Ran Liu. Radon mitigation strategy and results for the supernemo experiment. IoP APP / HEPP Conference, 2018.

- [15] A. Huber. *Recherche de la nature du neutrino avec le détecteur SuperNEMO : Simulations optiques pour l'optimisation du calorimètre et performances attendues pour le  $^{82}\text{Se}$* . PhD thesis, Université Bordeaux, 2017.
- [16] R. Arnold et al. Probing new physics models of neutrinoless double beta decay with supernemo. *Eur. Phys. J. C*, 2010.
- [17] Tretyak V.I. Ponkratenko O.A. and Zdesenko Yu.G. The event generator decay4 for simulation of doublebeta processes and decay of radioactive nuclei. *Phys. At. Nucl.*, 63:1282–1287, Jul 2000.
- [18] R. Arnold et al. Results of the search for neutrinoless double- $\beta$  decay in  $^{100}\text{mo}$  with the nemo-3 experiment. *Phys. Rev. D*, 2015.
- [19] Gomez-Cadenas et al. Physics case of supernemo with  $^{82}\text{se}$  source. Internal presentation, 2008.
- [20] R. Arnold et al. Final results on  $^{82}\text{se}$  double beta decay to the ground state of  $^{82}\text{kr}$  from the nemo-3 experiment. *Eur. Phys. J. C*, 2018.
- [21] Cousins D. Feldman G. A unified approach to the classical statistical analysis of small signals. *Phys.Rev.*, pages 3873–3889, 1999.
- [22] J. Kotila and F. Iachello. Phase-space factors for double- $\beta$  decay. *Phys. Rev. C*, 85:034316, Mar 2012.
- [23] Dong-Liang Fang, Amand Faessler, Vadim Rodin, and Fedor Šimkovic. Neutrinoless double- $\beta$  decay of deformed nuclei within quasiparticle random-phase approximation with a realistic interaction. *Phys. Rev. C*, 83:034320, Mar 2011.
- [24] A. Chapon. *Mesure des processus de double désintégration bêta du Mo vers l'état excité  $0_1^+$  du Ru dans l'expérience Nemo3, Programme de R&D SuperNEMO : mise au point d'un détecteur BiPo pour la mesure de très faibles contaminations de feuilles sources*. PhD thesis, Université Caen Basse-Normandie, 2011.
- [25] Snow S. A magnetic field map for the tracker. Internal presentation, 2015.
- [26] A. Pin. *Recherche de la nature du neutrino via la décroissance double bêta sans émission de neutrinos. Caractérisation et optimisation du calorimètre SuperNEMO et impact sur la recherche de la décroissance du  $^{82}\text{Se}$  Développement du premier prototype LiquidO*. PhD thesis, Université Bordeaux-Gradignan, 2020.
- [27] A. H. Wapstra G. Audi. The 1995 update to the atomic mass evaluation. *Nucl. Phys. A*, 595:409–480, feb 1995.
- [28] R. Arnold et al. Measurement of the  $2\nu\beta\beta$  decay half-life of  $^{150}\text{nd}$  and a search for  $0\nu\beta\beta$  decay processes with the full exposure from the nemo-3 detector. *Phys. Rev. D*, 94, oct 2016.

- [29] Nucleid database.